Tomographic imaging of bone composition using coherently scattered x rays[*]

D. L. Batchelar[1,2], W. Dabrowski[1], and I. A. Cunningham[1,2,3]

[1]Imaging Research Laboratories, John P. Robarts Research Institute,
P. O. Box 5015, 100 Perth Drive, London, Ontario, N6A 5K8, Canada
[2]Department of Medical Biophysics, University of Western Ontario,
London, Ontario, N6A 5C1, Canada
[3]Department of Radiology, London Health Sciences Centre, London, Ontario, Canada

Bone-tissue consists primarily of calcium hdroxyapatite-crystals (bone mineral) and collagen fibrils. Bone mineral density (BMD) is commonly used as an indicator of bone health. Techniques available at present for assessing bone health provide a measure of BMD, but do not provide information about the degree of mineralization of the bone tissue. This may be adequate for assessing diseases in which the collagen-mineral ratio remains constant, as assumed in osteoporosis, but is insufficient when the mineralization state is known to change, as in osteomalacia. No tool exists for the *in situ* examination of collagen and hydroxyapatite density distributions independently.

Coherent-scatter computed tomography (CSCT) is a technique we are developing that produces images of the low-angle scatter properties of tissues. These depend on the molecular structure of the scatterer, making it possible to produce material-specific maps of each component in a conglomerate. After corrections to compensate for exposure fluctuations, self-attenuation of scatter and the temporal response of the image intensifier, material-specfic images of mineral, collagen, fat and water distributions are obtained. The grey-level in these images provides the volumetric density of each component independently.

KEYWORDS: X-ray diffraction, computed tomography, material-specific imaging, bone-mineral density (BMD)

1. INTRODUCTION

Bones are comprised of hydroxyapatite (a calcium phosphate salt), collagen, yellow marrow (fat), and bloody marrow (water). The hydroxyapatite, or bone mineral, crystals are embedded in a collagenous matrix to form bone tissue.[1] This tissue provides bones with rigidity and strength as well as acting as a mineral store for the body as a whole. Metabolic bone diseases form a group of disorders that affect bone tissue. These diseases affect either structural homeostasis, as in osteoporosis and Paget's disease, or mineral metabolism, as in osteomalacia and hyperparathyroidism.[2] These effects are not independent. Bone mineral has both structural and metabolic functions so that disturbances in structure alter Ca metabolism and changes in Ca metabolism can lead to mechanical failure. For this reason, bone mineral density (BMD) is commonly used as an indicator of bone status, both structural and metabolic.[1]

Several radiographic technologies have been developed to measure BMD *in vivo*, including radiographic absorptiometry (RA), dual-energy x-ray absorptiometry (DEXA), and quantitative computed tomography (QCT). All of these are being used to diagnose and monitor osteoporosis, the most common bone disorder in North America.[3] Conventional x-ray techniques are, however, limited because they provide no information on the degree to which the tissue is mineralized. Such approaches are adequate when the collagen-hydroxyapatite ratio within the bone tissue remains constant, as is assumed in osteoporosis. Patients with osteoporosis are thought to have normally mineralized bone present in abnormally low volume. The traditional view of osteoporosis has been challenged in recent years by evidence suggesting that bone tissue normally becomes more highly mineralized with age.[4] Osteomalacia arises from vitamin D deficiency and results in poorly mineralized bone tissue. This will reduce an individual's BMD similar to

osteoporosis, but has a completely different etiology and may be indicative of renal or hepatobilary diseases. Osteomalacia is not definitively recognizable either by x-ray exam or densitometry: a bone biopsy is often required.[5] The relation between bone structure and function, as well as the invasiveness of the biopsy procedure, makes desirable the development of a non-destructive, *in situ*, technique for examining all bone components independently.

Coherent-scatter computed tomography is being developed to provide such a tool. This method is based on crystallography techniques that have been used for almost a century for the analysis of material composition. CSCT produces images based on the low-angle (0 - 10°) scatter from a sample. The cross-section for coherent scatter depends on the molecular structure of the scatterer and is, therefore, a unique signature of the material's electronic configuration. Furthermore, the cross-section of a composite material is just a linear superposition of the cross-sections of its components. Thus, the composition of a conglomerate can in principle be elucidated based on its coherent-scatter pattern. Each component of bone has a distinctive coherent scatter signature (Fig. 1). These indicate that it is possible to use CSCT images to non-destructively examine bone tissue.
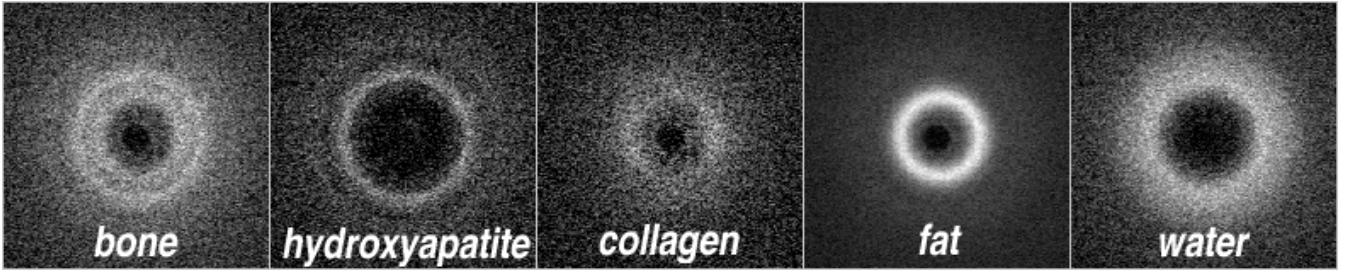

Figure 1:Scatter patterns obtained from a bone specimen and pure samples of hydroxyapatite, collagen, fat and water. The patterns display the circular symmetry characteristic of amorphous and polycrystalline materials. Comparing the bone pattern with those of its components clearly demonstrates that it is a superposition.

Previously, we have demonstrated that CSCT can identify the components of a plastic phantom[6,7] using a prototype CSCT scanner. Before this technique can be used to quantify bone mineral several issues must be addressed, as described in this article. Scatter from system components must be excluded from detection. The behaviour of all system components, which includes two radiation detectors and and x-ray image intensifier (XRII) with a CCD video camera, must be characterized and understood and any irregularities must be corrected for. One must ensure that all detectors respond linearly to variations in exposure. Finally, fluctuations in beam intensity must be compensated for, as must attenuation of scatter by the object.[7]

2. METHODS

2.1. System Description

The CSCT scanner (Fig. 2) is based on our proof-of-concept scanner which has been described previously.[8] Coherent-scatter is the weakest of photon interactions in the diagnostic energy range. It is, therefore, imperative to ensure that the signal detected is free of contamination by radiation from sources other than the scatterer. While it is impossible to eliminate high-energy photons from the natural background, it is possible to minimize the signal coming directly from the x-ray tube as well as that from scatter off system elements. To this end, the entire x-ray tube is shielded with 3 mm of lead while the exit window has an additional 3 mm. This shielding has a 5 mm diameter hole, centered on the focal spot, which prevents any off-focal radiation from interacting with system components. A third shield is mounted on the back face of the collimator to eliminate photons scattering off the exit hole of the shielding.

Mounted within the exit-window shielding is a 0.30 g/cm^2 Gd filter. This attenuates the primary by approximately 90% and reduces the spectral width from 27% to 14%, improving the angular resolution of the measured cross-sections.[8] After filtration, the beam is collimated to a 1 mm², square pencil-beam using a triple-aperture parallel-plate collimator. This arrangement minimizes the scatter from the front face of the collimator.
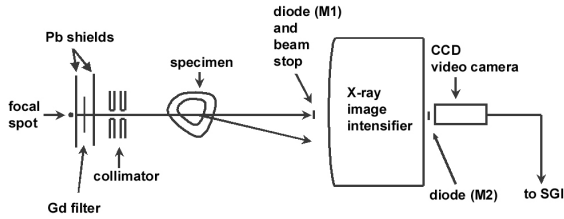
Figure 2: Schematic diagram of the system used to acquire coherent-scatter patterns.
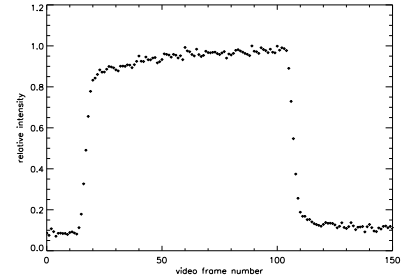

Figure 3: Temporal response of the XRII measured using M2. The intensifier was exposed to scatter from a homogeneous specimen. Ignoring variations in photon fluence, the response should be constant during the exposure. The deviation from this displayed here is due to decay constants in the XRII phosphors.

The specimen is mounted on a translate-rotate stage in front of the collimator, and is translated through the beam during a six second exposure. The coherent scatter from the object is detected by a diagnostic x-ray image intensifier (XRII) coupled to a CCD video camera. Specimen translation and CCD-video data acquisition are synchronous with an external video signal generator. The video data is digitized on an SGI O2 such that each video field corresponds to a known specimen position with an accuracy of 0.03 mm. The transmitted primary is blocked by 3 mm of lead and monitored by a detector consisting of a Kodak Lanex Fine (Gd_2O_2S) radiographic screen optically coupled to a Si-photodiode (M1). The intensity of the output phosphor on the XRII is also monitored with a Si-photodiode placed in the parallel beam of the optical path between the XRII and the CCD camera (M2). The signal from each photodiode is digitized on a PC at approximately 12 kHz, providing 200 samples of intensity per video frame, accurately synchronized to the video clock. The monitor signals are integrated and registered with the appropriate video frame.

2.2. XRII temporal response

The image intensifier provides an output signal that is linearly related to the input, but is subject to lag due to decay time constants within the input and output phosphors[9,10] (Fig. 3). We examine the intensifier data on a frame-by-frame basis at a rate of 30 frames per second. Under these conditions, the relatively slow response of the XRII will be misinterpreted as an erroneous scatter intensity and an incorrect density determination will result.

Temporal lag is described in terms of a temporal impulse response function. Thus, to correct for lag in our data, we treat the XRII signal as an "ideal" signal (a signal without lag) convolved with a response function. To determine the appropriate response function, we used data from the photodiode monitoring the XRII output phosphor. The function, $R(t)$, displayed in Fig. 4, was calculated using the rising portion of the curve found in Fig. 3. In principle, lag could be removed by deconvolving the measured signal using the response function $R(t)$. However, deconvolution can be unstable and we have developed an approximate correction instead.

The response of the XRII output signal to variations in scatter intensity is shown below to be linear. Therefore, we can write

$$M(t) = T(t) * R(t) \qquad (1)$$

where $M(t)$ is the measured signal and $T(t)$ is the true signal. This allows us to determine the error, $E(t)$, in each video frame as the difference between the measured and true signals:

$$E(t) = T(t) - T(t) * R(t). \qquad (2)$$

We cannot, however, determine the true output response. We do know that the error in each frame is not large ($< 10\%$, generally) so we can say that $M(t) \approx T(t)$ and use our measured signal to calculate the error in each frame:

$$E(t) \approx M(t) - M(t) * R(t). \tag{3}$$

Thus, the corrected signal is just $M'(t) = M(t) + E(t) \approx T(t)$.

This procedure was tested on simulated data and then implemented in our analysis using diode M2 to determine the error and applying a multiplicative correction to the intensifier data, $I(x, y, t)$. To be perfectly rigorous, this correction should be applied on a pixel by pixel bases. This would, however, be computationally intensive and our data does not vary widely enough across a video frame to warrant the time expenditure this would require. A single correction factor is applied to the whole of each video frame.

$$I'(x, y, t) = I(x, y, t) \times \frac{M'(t)}{M(t)} \tag{4}$$

where $I'(x, y, t)$ represents the XRII data corrected for time lag. This method only corrects for the effect of lag on a time scale of approximately 1.7 s or less.
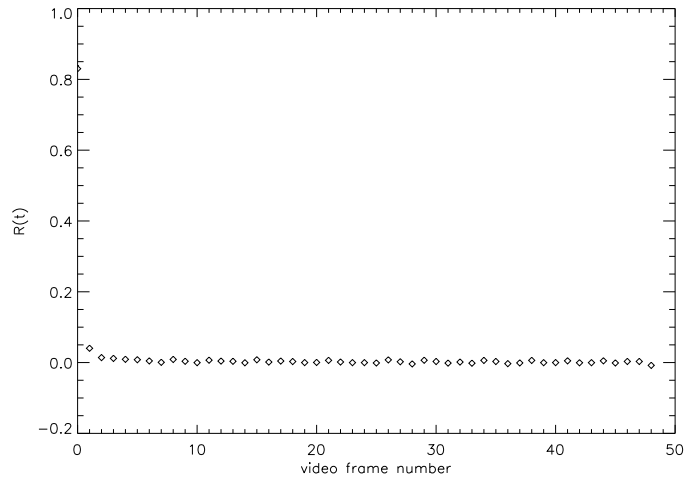

Figure 4: The response function used to correct the XRII data, R(t).

2.3. Self-attenuation

Attenuation of scattered x rays by the scatterer results in an apparent signal drop in the centre of large objects.[7] This effect manifests as a cupping artifact in CSCT images and can lead to systematic errors of up to 20% in cross-sections measured from these images. Self-attenuation is easily corrected for by normalizing the video data $I(x, y, t)$ to the transmitted primary $P(t)$ on a frame by frame basis, after correcting for lag:

$$I_{corr}(x, y, t) = \frac{I'(x, y, t)}{P(t)} \tag{5}$$

2.4. System linearity

The corrections described above are valid only for linear systems. We examined the relative response of each detector to varying input intensities. This was accomplished by acquiring six seconds of scatter data from a 1 cm Lucite block at four different current settings (10, 25, 50, and 100 mA, nominal). The intensifier and diode (M2) data were corrected according to Eq. (4). The recorded intensities were normalized to the largest value in each data set respectively.

To test the quantitative accuracy of the scanner, a simple model was used. Data was acquired from a series of Lucite sheets varying in thickness from 2 mm to 12 mm in 2 mm increments, as well as from one 5 mm thick, and corrected for lag and self attenuation. Cross-sections were obtained from each sheet.[8] The 5 mm cross-section was used as a basis function, and the appropriate scaling factors relating the basis function to all other cross-sections were determined using a non-negative least squares algorithm. These scaling factors reveal the fraction of the basis function present in each sheet and allowed us to determine the thickness of each using our technique.

2.5. Bone specimen

CSCT images of a frozen, excised pork rib were acquired at 70 kVp, 100 mA. These exposure settings resulted in an average total dose of approximately 10 mSv delivered to the specimen. This is a factor of 10 less than that achieved using our proof-of-concept system,[6] due to optimizations made in the video-system for low-noise acquisition. The scatter patterns acquired were corrected for lag and normalized to the measured transmitted intensity to compensate for attenuation of scatter within the specimen.[7] The patterns were then analyzed as described in Westmore *et al.*[6] to obtain coherent-scatter cross-sections for each pixel in a slice through the specimen. Cross-sections for water, fat, collagen and hydroxyapatite were acquired from pure samples of known density and were used as a set of basis functions. The pixel cross-sections were decomposed into linear combinations of these basis functions. The fit parameters determined for each material indicate the fraction, by density, of each basis density present in each pixel. This results in an independent map of the density, in g/cc, of each component present.

3. RESULTS

The images in Fig. 5 illustrate the residual scatter from system components. When no scatterer is present, a small signal is seen immediately surrounding the beam-stop. This is believed to be scatter from the block. The strength of the signal is, however, only 1% of the scatter strength when a 1 cm specimen is in place. At this level, and with the signal confined to a tight ring, it is possible to simply subtract it from the scatter patterns.
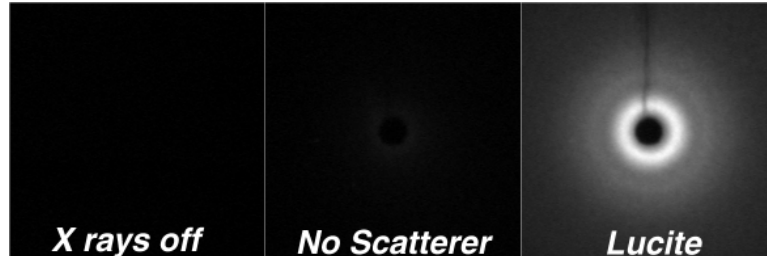

Figure 5: Intensifier signal with no x rays, x rays on but no scatterer, and with 1 cm of Lucite.

3.1. XRII temporal response

The temporal lag correction was tested first on simulated data (Fig. 6). An ideal box function was convolved with our temporal response function (Fig. 4) to mimic lag in the intensifier. The output was then used to determine the error on each video frame and the corrected output was calculated. The small residual error evident in Fig. 6 demonstrates that our approximation reduces the effect of lag from approximately 18% to an acceptable level of approximately 2%
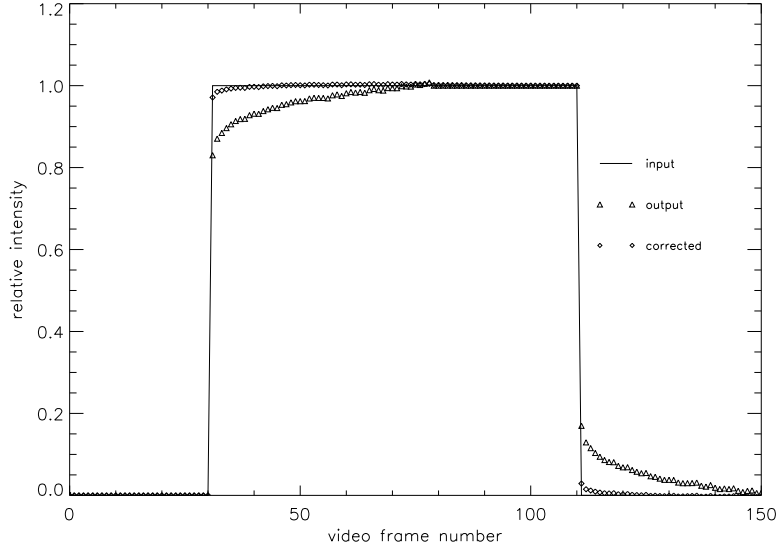
Figure 6: Test of the validity of the temporal lag correction using simulated data.

The correction was then applied to real data acquired as a block of Lucite passed through the beam. This case is not identical to the simulated case because it does not result in an instantaneous change in signal. The scatter intensity will grow to full intensity as the object moves fully into the beam. After this, ignoring fluctuations in x-ray intensity, the scatter signal should be constant across the scan, then fall to background as the object moves out of the beam. This is illustrated in the transmitted primary (M1) curve in Fig. 7. The curve is, of course, inverted because it is an attenuation signal. The small rise at the beginning of the M1 curve is due to an overshoot in x-ray tube output, which rapidly settles to a stable level.
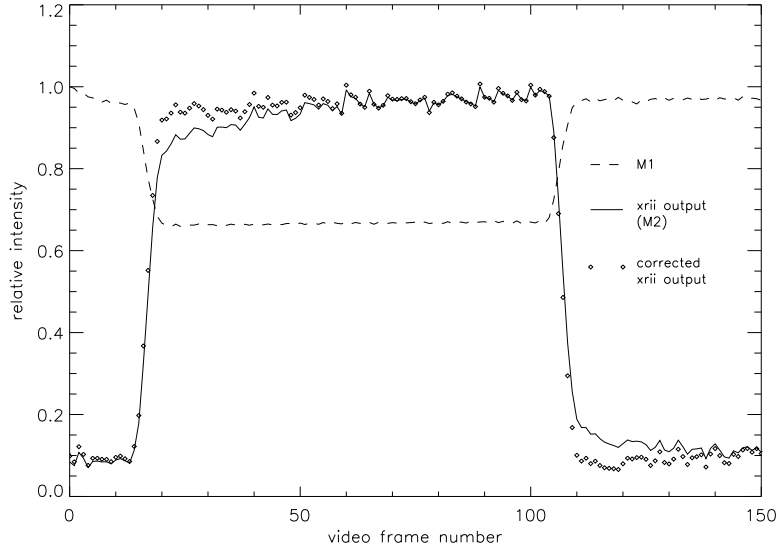

Figure 7: Intensifier data for the translation of a piece of Lucite through the x-ray beam, before and after correction. The monitored primary transmission (M1) data is also included.

The XRII data in Fig. 7 clearly exhibits temporal lag. The corrected curve shows considerable improvement. It can be observed that both the corrected and uncorrected data continue to rise throughout the object's transit. We have no means of knowing what the true signal should be. We do know that a uniform object was used to generate the data. Thus, the slope of the data for the portion of the curve with maximum scatter should be zero. Prior to correction the slope was 0.0017 intensity units/video frame. After correction the slope is reduced by more than a factor of three, to 0.00052 intensity units/video frame. The residual slope is believed to be due to components in

the XRII temporal response greater than approximately 1.7 s, which are not corrected for using our approximate method. Another contributing factor may be variations in x-ray output during the translation. The slope of the equivalent portion of the m1 curve is 0.00012 intensity units/video frame, indicating that this is the case.

3.2. System linearity

The results of characterizing the relative response of the detectors are displayed in Fig. 8. Results for the intensifier and diode M2, after temporal correction, are plotted against those of the transmitted primary. This was done because there is no absolute current reading for the generator used. The transmitted primary was chosen as the ordinal because no correction is applied to this data. It is clear that the detectors, M1, M2, and the XRII, are linear with respect to each other. The equation of the intensifier curve is $y = 1.004x - 0.002$, and that of the second diode is $y = 1.009x + 0.002$. These results indicate that no adjustments to Eq. (5) are required to account for tube output fluctuations.
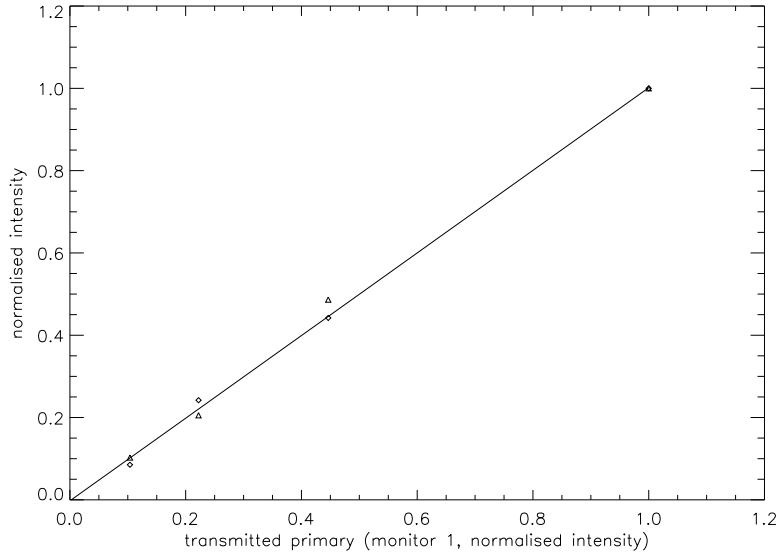

Figure 8: Demonstration of linearity of M2 (triangles) and XRII (diamonds) for changes in exposure mA.
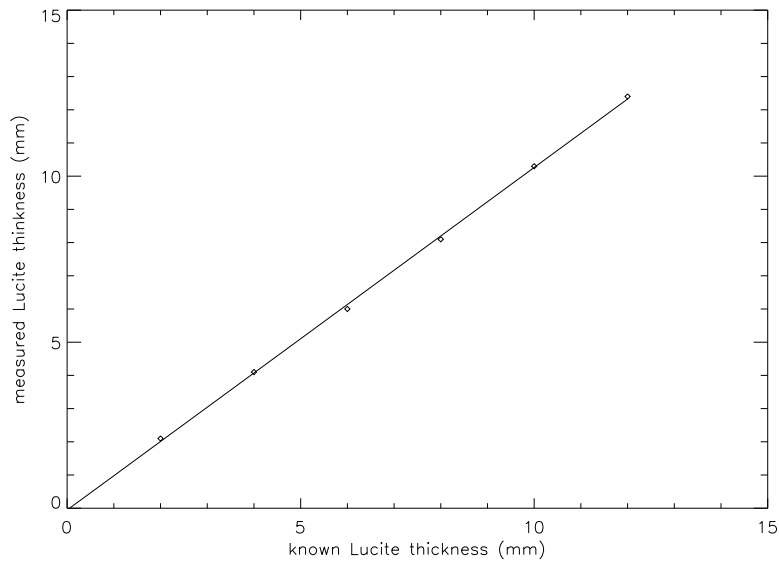

Figure 9: Thickness measurements for six sheets of Lucite, from 2 to 12 mm thick.

Figure 9 contains the results of the test of quantitative accuracy. The equation of this line is $y = 1.03x - 0.05$, demonstrating not only that we can quantify the thickness of materials with our scanner, but also that the system responds linearly to variations in the number of scatterers present in the specimen. Furthermore, this demonstrates that we are using an acceptable lag correction and are adequately compensating for self-attenuation. This data is the first absolute quantification obtained using our CSCT scanner.

3.3. Bone Specimen

Volumetric density maps of each bone component are displayed in Fig. 10. The images all closely reflect the expected anatomy. The fat distribution is limited to the medullary canal. No significant water content was measured. This was expected as the bone had been drained of blood, the strongest source of water signal in a bone. In the marrow space, the collagen and fat distributions appear to be complementary. It is not clear at present whether this is anatomically correct or due to the effect of noise in the analysis. The hydroxyapatite is found in the cortical region as is collagen. Comparison of the collagen and hydroxyapatite distributions shows the expected spatial relation between bone mineral and its matrix. The densities displayed in Fig. 10 lie within reasonable physiological bounds, but have not been confirmed by independent analysis. These are the first tomographic images of any kind displaying the independent, volumetric density distributions of collagen and hydroxyapatite.
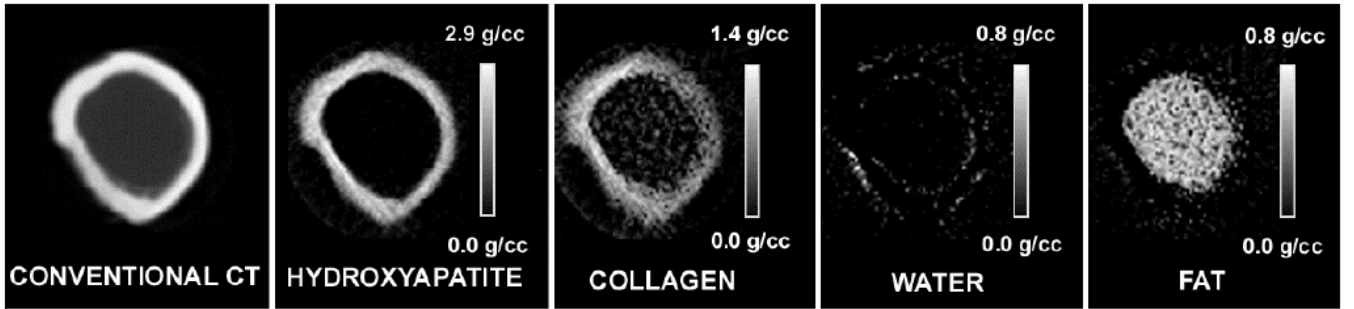

Figure 10:Material specific images of bone and its components.

4. CONCLUSIONS

Image intensifier data is subject to temporal effects due to delays in the phosphor screens, known as lag. In CSCT, where video data is acquired at 30 frames per second, lag is an impediment to obtaining accurate measures of the scatter intensity at all time points. It has been demonstrated that an approximate correction for the intensifier temporal response, where an estimate of the error in each video frame is determined using the video data alone, provides a significant improvement in our measurements (Fig.6 and Fig.7). After applying this correction, it is possible to ignore the residual effects of lag in CSCT data.

By examining the scatter intensity from a 1 cm block of Lucite at four different tube currents, we were able to demonstrate that the system responds linearly to variations in signal intensity (Fig. (8)). The intensifier signal changes with a slope of 1.004 with respect to the transmitted primary, while M2 varied with a slope of 1.009. In both cases the intercept was 0.002 normalized intensity units. The M2 and XRII data were corrected for lag before analysis so these results indicate not only that the detector chain is linear, but also that the temporal correction is being applied correctly. The quantitative response of the scanner was tested on a simple model consisting of a series of Lucite blocks. The results of this test (Fig. 9) demonstrate that the CSCT technique can accurately assess the quantity of material under interrogation.

The volumetric density maps displayed in Fig. 10 illustrate the potential of CSCT imaging. These are the first tomographic images of their kind. Each image gives the density distribution of a component of bone independent of all other elements and each is anatomically accurate. Careful examination of the fat and collagen images reveals that they are complementary. This may be physiologically real, as marrow fat cells are embedded in a loose collagenous

matrix, or it may be a manifestation of structured noise in the material-specific images. Resolution of this issue requires further investigation.

We are developing CSCT to provide a means of determining the volumetric density of each component of a tissue specimen at each point in a tomographic slice. This is accomplished by determining the coherent-scatter cross-section for each pixel in an image and fitting it with a set of basis cross-sections from pure samples of each material present. When the densities of the basis samples are known, the fit parameters indicate the fraction of the basis density present in each pixel. For these measurements to be accurate, the structure and magnitude of the measured cross-sections must be accurate. This requires that one reduces the background signal as much as possible to reduce any offset in the measured cross-sections. The detectors used must be completely characterized and any non-idealities compensated for, and the raw data must be adjusted to correct for exposure fluctuations and self-attenuation of the scatter.[7] This paper described the system characterization process and presented results demonstrating the quantitative results achievable using CSCT.

5. ACKNOWLEDGEMENTS

REFERENCES

1. R. E. Baron, "Anatomy and ultrastructure of bone," in *Primer on Metabolic Bone Diseases and Disorders of Mineral Metabolism*, M. J. Favus, ed., pp. 3–10, Lippincott-Raven, Philedelphia, 3 ed., 1996.
2. L. Lenchik and D. J. Sartoris, "Orthopedic aspects of metabolic bone disease," *Orth. Clin. North Am.* **29**, pp. 103–134, 1998.
3. S. Grampp, H. K. Genant, A. Mathur, P. Lang, M. Jergas, M. Takada, C.-C. Gluer, Y. Lu, and M. Chavez, "Comparisons of noninvasive bone mineral measurements in assessing age-related loss, fracture discrimination and diagnostic classification," *J. Bone Miner. Res* **12**, pp. 697–711, 1997.
4. M. Grynpas, "Age and disease-related changes in the mineral of bone," *Calcif. Tissue Int.* **53 (Suppl 1)**, pp. S57–S64, 1993.
5. E. Bonucci, "Bone biopsy in metabolic bone disease," in *Bone Densitometry and Osteoporosis*, H. K. Genant, G. Guglielmi, and M. Jergas, eds., pp. 173–191, Springer-Verlag, Berlin, 1998.
6. M. S. Westmore, A. Fenster, and I. A. Cunningham, "Tomographic imaging of the angular-dependent coherent-scatter cross section," *Med. Phys.* **24**, pp. 3–10, 1997.
7. D. L. Batchelar, M. S. Westmore, H. Lai, and I. A. Cunningham, "Quantitative coherent-scatter computed tomography," *Proc. SPIE* **3336**, pp. 707–715, 1998.
8. M. S. Westmore, A. Fenster, and I. A. Cunningham, "Angular-dependent coherent scatter measured with a diagnostic x-ray image intensifier-based imaging system," *Med. Phys.* **23**, pp. 723–733, 1996.
9. R. K. Swank, "Absortion and noise in x-ray phosphors," *J. Appl. Phys.* **44**, pp. 4199–4203, 1973.
10. J. A. Rowlands, "Videofluorography: The role of temporal averaging," *Med. Phys.* **11**, pp. 129–136, 1984.